Rectification and Photoconduction Mapping of Axial Metal-Semiconductor Interfaces Embedded in GaAs Nanowires

Marta Orrù,[1] Vincenzo Piazza,[2] Silvia Rubini,[1] and Stefano Roddaro[1,3,*]

[1]*Istituto Officina dei Materiali CNR, Basovizza SS 14 km 163.5, I-34149 Trieste, Italy*
[2]*Center for Nanotechnology Innovation @NEST, Istituto Italiano di Tecnologia,*
Piazza San Silvestro 12, 56127 Pisa, Italy
[3]*NEST, Scuola Normale Superiore and Istituto Nanoscienze-CNR,*
Piazza San Silvestro 12, I-56127 Pisa, Italy

Semiconductor nanowires have emerged as an important enabling technology and are today used in many advanced device architectures, with an impact both for what concerns fundamental science and in view of future applications. One of the key challenges in the development of nanowire-based devices is the fabrication of reliable nanoscale contacts. Recent developments in the creation of metal-semiconductor junctions by thermal annealing of metallic electrodes offer promising perspectives. Here, we analyze the optoelectronic properties of nano-Schottky barriers obtained thanks to the controlled formation of metallic AuGa regions in GaAs nanowire. The junctions display a rectifying behavior and their transport characteristics are analyzed to extract the average ideality factor and barrier height in the current architecture. The presence, location, and properties of the Schottky junctions are cross-correlated with spatially resolved photocurrent measurements. Broadband light emission is reported in the reverse breakdown regime; this observation, combined with the absence of electroluminescence at forward bias, is consistent with the device unipolar nature.

I. INTRODUCTION

Self-assembled nanowire (NW) synthesis represents today a mature and promising approach to the fabrication of advanced nanodevices [1,2] with a potential impact on electronics [3–9], photonics [10–14], and spintronics [15–18] applications. These perspectives stem from the flexibility of this growth technique, that allows the fabrication of advanced bottom-up nanostructures in many copies and without the need of advanced lithography. Thanks to their limited radial dimensions, NWs can accommodate a much larger-than-usual lattice mismatch without the nucleation of dislocations, since strain can be relaxed very effectively in the radial direction [19–21]. This allows the achievement of a wide range of single-crystal heterostructures [22–25] as well as the integration of mismatched III-V materials on the more standard Si-based technology [26,27].

A further promising development direction has emerged in recent years following the demonstration of NWs combining metallic and semiconductor regions. Such a possibility has been first highlighted in the seminal work by Wu *et al.* [28], who demonstrated that full portions of a Si NW can be converted into crystalline SiNi by a suitable thermal annealing of Ni contacts. More recently, this technique was further refined [29–31] and exploited to implement a variety of novel NW-based circuit elements

such as reconfigurable logic gates [31], ultrashort-channel field-effect transistors [30,32], and more [33]. Recently, the range of semiconductor materials displaying similar phenomenology was extended [34]. In particular, some of us have demonstrated the formation of sharp axial metal-semiconductor junctions starting from III-V NWs [35]. In GaAs NWs, metallic Au-rich regions can be in fact induced deep inside the crystal by rapid thermal annealing of a suitable Au-based electrode multilayer.

The development of this class of *ex situ* solid-state reactions offers a way to tailor the transport in individual nanostructures and to create nanometer-scale electrical contacts [28–35]. Among the advantages of this approach are the following. (i) Since junctions are obtained by thermal migration of metallic species, no surface-oxide issues are expected to impact the electrical behavior of the semiconductor-metal interface. (ii) Contacts with cross-section dimensions of a few nanometers can be easily obtained without the need of advanced lithography and without stray capacitive effects due to large-scale electrodes, with a potential benefit for high-speed applications [13]. (iii) The junction position along the NW can be controlled by tuning the thermal annealing protocol, again leading to a nanometer-scale control without the need of advanced lithography [30,32]. The structural and electrical properties of this class of nanojunctions are still under active investigation. Transmission electron microscopy studies indicate, in the more extensively explored case

[*]s.roddaro@sns.it

of SiNi, that various metallic alloys with different stoichiometries can be formed depending on the fabrication protocol, and that a good degree of crystallinity can be achieved at the junction [36,37]. From the charge-transport point of view, in the case of SiNi, junctions often display a Schottky-like behavior and have been exploited to build a variety of device architectures [29–31]. Regarding III-V semiconductors in general, and GaAs NWs in particular, traditional nanoscale junctions are so far typically obtained using an epitaxy of radial [38] and axial [39] *p-n* junctions or the AuIn nanoparticle seeding the growth [40,41]. Thermally induced metal-semiconductor junctions were in fact only recently demonstrated [35]. In this context, III-V semiconductors are particularly promising in view of the advanced NW heterostructures that can be implemented with these material systems [13,15–17,22] and thanks to the large mobility and optically active gaps that can be obtained in III-V semiconductors.

In this paper, we investigate the fundamental optoelectronic properties of GaAs-metal nanojunctions obtained by thermal annealing. Transport spectroscopy and photoconductivity (PC) microscopy are performed on devices that allow—thanks to the parallel fabrication of standard Ohmic contacts to the GaAs NW body—studying the optoelectronic properties of individual axial metal-GaAs heterojunctions. Studied devices display a marked rectifying behavior, which is due to the formation of a Schottky barrier between the pristine GaAs NW body and the newly formed Au-rich regions. Experimental results indicate an ideality factor $\eta = 2.3$–3.3 and the presence of a Schottky barrier with an estimated height of about 500 meV. The unipolar nature of the device is consistent with the absence of light emission in normal forward bias. Differently, a pointlike broadband emission [42–44] is observed in the reverse breakdown regime, with an emission spot consistent with the position of the junction.

II. EXPERIMENT AND DISCUSSION

The architecture of the NW Schottky diodes is visible in Fig. 1 and is based on the creation, by thermal annealing, of an axial metal-semiconductor heterointerface inside the nanostructure. GaAs NWs are grown by means of catalyst-free molecular beam epitaxy (MBE), at a beam pressure ratio As/Ga equal to 5 [45]. A GaTe source is used to achieve a strong *n*-type doping. NWs had an average diameter of 100 nm, a length up to 6 μm, and a nominal doping level of the GaAs NWs is estimated to 8.5×10^{19} cm^{-3} from field-effect measurements [46,47]. As-grown NWs are dispersed by sonication in isopropyl alcohol and deposited by drop casting on prepatterned chips made of heavily *p*-doped Si(100) substrates covered with 300 nm of SiO$_2$, which could also act as a back gate. The contacts on top of each NW are defined by *e*-beam lithography and metal evaporation. As depicted in the sketch of Fig. 1(a), the devices included three contacts
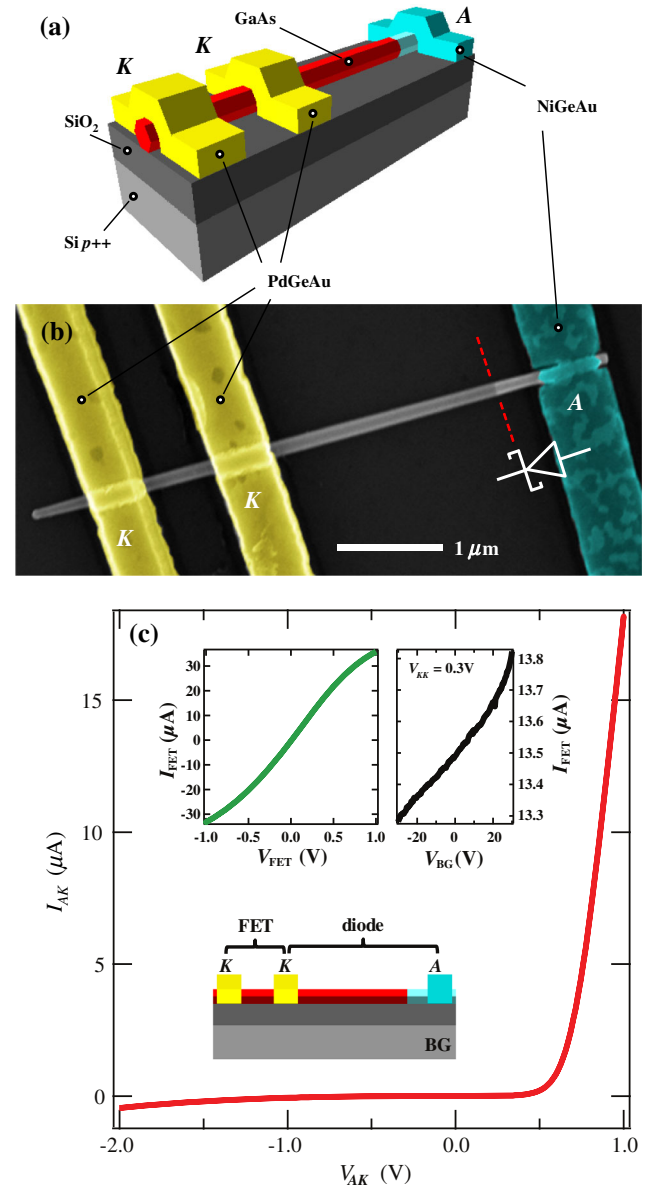
FIG. 1. *Device architecture*. (a) Sketch of the device structure. The *n*-type GaAs nanowire is deposited on a Si/SiO$_2$ substrate acting as a back gate, and contacted by two different multilayer electrodes: PdGeAu for the cathode (K) and NiGeAu for the anode (A), *diode* bias configuration. Upon thermal annealing, a Au-rich region is formed inside the nanowire, with a Schottky interface with the pristine GaAs. (b) Scanning electron micrograph of one of the Schottky diodes. The Au-rich region is visible as a brighter region of the nanowire and the interface with the pristine GaAs marked by the red dashed line. (c) The device displays a strong rectification as a function of the voltage between A and K, V_{AK}. Inset: current-voltage characteristics of pristine GaAs, measured between two K Ohmic contacts (left, FET bias configuration); evolution of current as a function of the back-gate voltage V_{BG} at bias 0.3 V (right).

on each GaAs NW, obtained with a two-step fabrication procedure. In a first lithographic step the device anode (A) is defined. The contact region is first cleaned in an oxygen plasma and chemically passivated for 1 min in a

$HCl:H_2O$ (1:4) solution. Immediately after, a Ni(4 nm)/ Ge(40 nm)/Au(20 nm)/Ni(15 nm)/Au(40 nm) multilayer is deposited by e-beam evaporation (cyan in Fig. 1). After lift-off, rapid thermal annealing in a N_2 environment for 3 min at 360 °C led to the formation of a Au-rich region with no visible change in NW morphology [35]. The exact nature and stoichiometry of this alloy is still under investigation, but available energy-dispersive x-ray spectroscopy data [35] indicate a clear predominance of Au and Ga. In the rest of the paper, we will thus refer to this NW portion as the "AuGa region." After the first contacting procedure, the sample is again processed for the fabrication of two Ohmic contacts on the cathode (K) side using a Pd(50 nm)/Ge(150 nm)/Au(60 nm) multilayer (yellow in Fig. 1) recipe reported in the literature [48]. In this case, the contact electrodes are annealed again in a N_2 environment for 30 sec at 290 °C. No further surface passivation is performed on the NWs at the end of the fabrication. A representative final device is visible in the scanning electron microscope image of Fig. 1(b). In the picture, the formation of a AuGa phase can be recognized as a contrast step along the GaAs NW [35] and the interface between the GaAs pristine region and the new AuGa phase is marked by a red dashed line. As demonstrated in the following, the resulting device is an axial nanoscale Schottky diode with a rectifying junction located at the boundary between the AuGa region and the pristine GaAs NW.

The nature of the two different kinds of contacts is first of all tested by transport measurements at room temperature. I-V curves of a representative device are shown in Fig. 1(c). Each device is equipped with two distinct PdGeAu electrodes to implement a standard NW field-effect transistor (FET) and check the effective formation of proper Ohmic contacts to the NW. The linear behavior of the I-V characteristics measured in the FET configuration (see left inset) confirms that this is indeed the case. We tested devices with random orientation of the NW tip with respect to the contact scheme and for all of them the PdGeAu contacts are found to be Ohmic. The gate response of the FET is visible in the right inset. The dependence of the current as a function of V_{BG} confirms the NW has a n-type behavior as expected for our Te-doped GaAs NWs. The variation of the current in the channel is 3.7% over a range of ±30 V, consistently with a high doping level in the wires. No multiple A contacts are included in the current device architecture since the AuGa region of the NW is known to have a metallic behavior with a low-resistance contact with the NiGeAu metallizations. Two-wire measurements indeed typically yield a resistance of the order of 100 Ω and no field effect [35]. Further four-wire measurements indicate a conductivity for the AuGa region of the order of 10% of one of gold. The junction between the metallic AuGa region and the pristine GaAs is generally expected to give rise to a Schottky contact. Considering the

GaAs affinity $\chi_{GaAs} = 4.07$ eV and the work functions $\phi_{Au} = 5.1$–5.47 eV and $\chi_{Ga} = 4.32$ eV, a barrier $\phi_B \gtrsim 0.25$ eV can be expected—at first approximation—based on the Schottky-Mott rule [49]. In a real system, interface states are expected to further impact band alignment and in GaAs they are typically expected to pin the chemical potential close to the middle of the band gap. The I-V characteristics of the diode are visible in the main panel of Fig. 1(c). Given the high conductivity of the AuGa region, the nonlinear characteristics between contacts A and K can be safely attributed to the axial metal-semiconductor junction embedded in the NW. The diode threshold is typically observed at $V_{th} \approx 0.5$ V and beyond this point the device resistance quickly saturates to a linear regime with a slope of tens of kilo-ohms (≈ 18 kΩ in the case reported in Fig. 1) because of the intrinsic resistance of the pristine GaAs NW. Ten different diode devices are investigated, all displaying completely similar transport signatures to the ones reported in the paper, except for one diode having an almost symmetric nonlinear I-V curves, likely due to unideal PdGeAu contacts. Photoconductivity mapping is performed on three devices.

A more detailed transport analysis is reported in Fig. 2, where the ideality factors η and barrier heights ϕ_B are analyzed using a phenomenological model based on the Richardson equation for thermoionic emission above the barrier [49], with the inclusion of a series resistor R_S

$$V_{AK} = V_J + R_S I_{AK}, \tag{1}$$

$$I_{AK} = I_0[e^{qV_J/\eta k_B T} - 1], \tag{2}$$

$$I_0 = \Sigma \times \frac{4\pi q m^* k_B^2}{h^3} T^2 e^{-q\phi_B/k_B T}. \tag{3}$$
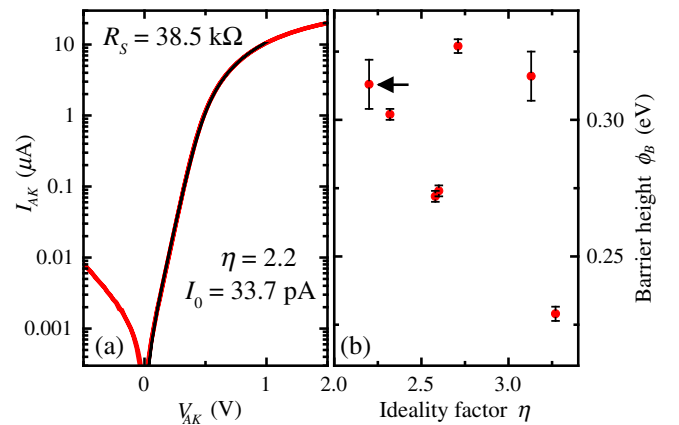
FIG. 2. *Nanodiode characteristics*. (a) Semilog plot of one of the diode's current-voltage characteristics. A fit using a thermoionic emission model yields a value for the barrier height ϕ_B, the ideality factor η, and the series resistance R_S. (b) Summary plot of the ideality factors η and barrier height ϕ_B obtained for the analyzed devices. The arrow indicates the fit parameters obtained from data in panel (a).

In Eqs. (1)–(3) V_J indicates the voltage drop over the junction, Σ is the NW cross-section area, m^* is the effective mass of GaAs, while q, k_B, and h are the electron charge, the Boltzmann constant, and the Planck constant, respectively. As visible in Fig. 2(a), the model provides a good fit of the forward bias portion of the I-V curve, but it fails to reproduce the negative branch because of a sizable non-linear resistive leak at the junction. This effect is likely due to tunneling and/or surface effects which are not taken into account by our phenomenological model. A further discussion about these effects and about the impact of thermionic field emission is reported in the Supplemental Material [47]. In Fig. 2(b), the results from the analyzed devices are reported: estimated η and ϕ_B values fall in the 2.3–3.3 and 0.2–0.35 eV range, respectively, with errors on ϕ_B mostly due to the uncertainty in the determination of Σ (estimated from scanning electron microscope imaging of the devices). We note the reported η values are larger than those expected for an ideal planar Schottky junction ($\eta = 1$), but this is not surprising in the case of nanoscale junctions. Large η values (up to the order of 10) have been typically reported for nanoscale Schottky contacts [50] due to tunneling [49], barrier lowering effects [51], and to the likely inhomogeneous band profile along the radius of the nano-devices caused by Fermi pinning at the surface [47,52]. The unipolar nature of the devices is also consistent with the absence of radiative recombination in the forward bias regime. This implies either that transport in the device does not involve minority carriers or that nonradiative recombination is strongly dominant. This is, however, not expected for GaAs and broadband radiation is indeed obtained in the strong reverse bias regime [47], in agreement with the literature [42].

In order to further clarify the origin of the rectifying behavior, PC maps are measured at room temperature on selected devices. In the semiconductor, a strong current response is in fact expected from regions characterized by a strong electric field, which promotes the separation of photogenerated electron-hole pairs [53]. Maps are taken by mounting the device on a piezoelectric stage and by scanning the sample under a focused laser beam (488 nm, 1 mW, spot size $\approx$0.5 μm, 63$\times$ objective with NA 0.75). The diode current is measured at one of the two PdGeAu electrodes, while applying a V_{AK} bias to the NiGeAu electrode [see inset to Fig. 3(a)]. The effect of the laser excitation is visible in Fig. 3(a), where we report a sequence
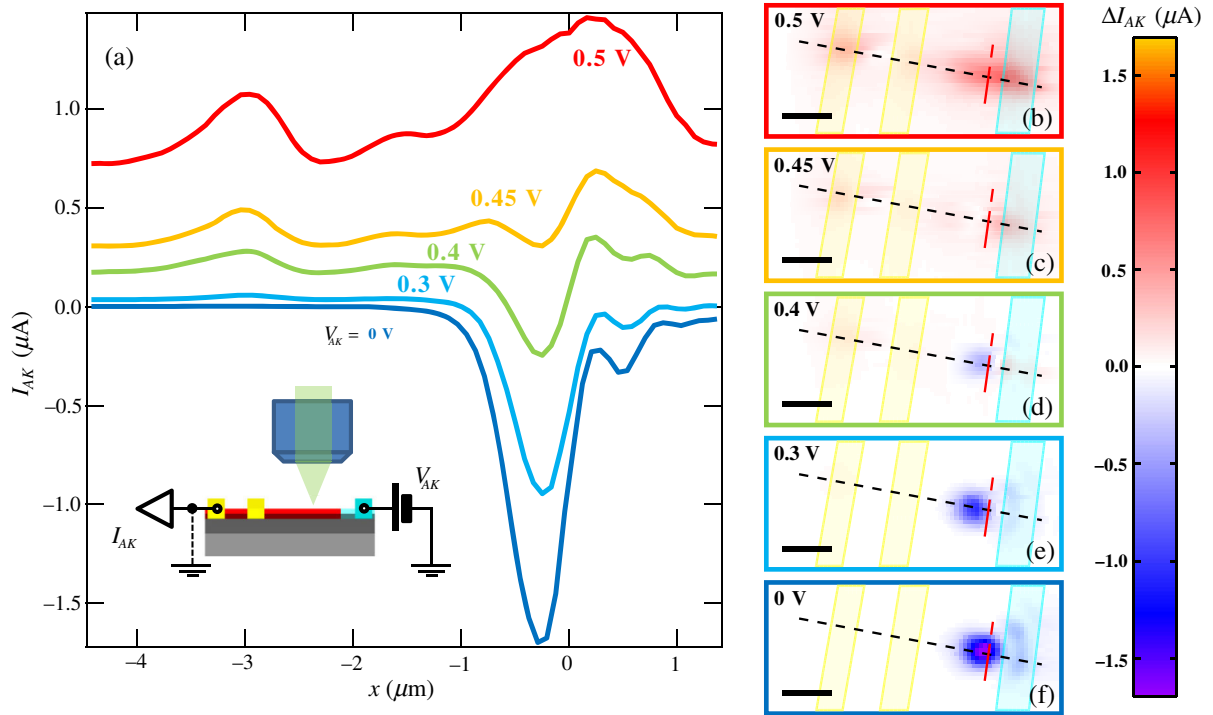
FIG. 3. *Photoconduction.* (a) Photocurrent I_{AK} profiles as a function of the laser position x along the nanowire with respect to the GaAs-AuGa interface, for selected values of the diode bias V_{AK}. The measurement scheme is sketched in the inset. Maps are obtained by scanning the device position under a 488-nm laser with a power of 1 mW and a spot size of 0.5 μm. The behavior of the photocurrent confirms the presence of a Schottky barrier at the junction at $x = 0$. Profiles are obtained as cross sections of the two-dimensional current maps which are plotted in panels (b)–(f) in terms of *excess* current ΔI_{AK} with respect to the value obtained when the laser spot is located far from the nanowire. The dashed red lines indicate the position of the Schottky interface and yellow (cyan) overlay polygons indicate the position of the PdGeAu (NiGeAu) electrode, based on a calibration done comparing the optical and electron microscope images of the device. Black scale bars correspond to 1 μm.

of I_{AK} current profiles as a function of the position x of the laser along the NW axial direction, where $x = 0$ corresponds to the Schottky junction position. The profiles are obtained from the two-dimensional PC maps visible in Figs. 3(b)–3(f), which are measured at selected values of V_{AK} and are plotted in terms of the excess current ΔI_{AK} induced by the laser. Excess current is here defined with respect to the V_{AK}-induced current measured when the laser is positioned far from the NW. In the panels, semitransparent yellow (cyan) overlays indicate the position of the PdGeAu (NiGeAu) electrodes and the red dashed lines indicate the position of the Schottky interface, as calibrated by comparing the laser position in the optical images acquired at the beginning and at the end of the measurement of the PC maps.

Measurements at $V_{AK} = 0$ V indicate the presence of a large electric field pointing in the $K \to A$ direction, inducing a negative photocurrent output at the K contact ($I_{AK} < 0$). The position of the negative current peak is consistent with the presence of a depletion region in the semiconductor NW at the interfacial region between the AuGa phase and the pristine GaAs NW and confirms the presence of a Schottky barrier between a metal and an n-type semiconductor [54]. The dimension of the depletion region is expected to be very small for the current highly doped GaAs NWs and thus cannot be evaluated from the PC maps because of their limited spatial resolution (the laser spot size is estimated to be 500 nm in the current setup).

An interesting evolution is observed when V_{AK} is increased up to and beyond the diode conduction threshold. The most prominent experimental feature observed in the PC maps is the quenching of the Schottky photocurrent peak. This is again consistent with our device model and indicates that the in-built electric field at the junction is reduced and even reversed at $V_{AK} \approx 0.4$–0.5 V, in agreement with the diode I-V characteristics. Below the threshold bias the Schottky junction is by far the most resistive portion of the device. We can thus roughly relate the 400–500-meV range to the height of the Schottky barrier in this device. This further suggests Φ_B parameters extracted from the I-Vs using the Richardson model are underestimated. An additional relevant effect is the emergence of a positive PC peak at the location of the K (PdGeAu) contact. Its presence and behavior as a function of V_{AK} can be explained in terms of a residual barrierlike behavior of the Ohmic contacts, which can be modeled by a diode D_K shunted by the contact resistance R_K (see schematics in Fig. 4). This is not in contrast with the previous assumption of an Ohmic behavior of the K contact, which is, in any case, much more conductive than the rest of the diode. As long as $V_{AK} \lesssim V_{th}$ the diode D_J is poorly conductive and much more resistive than the NW (R_{NW}) and than the K contact, which is expected to have a residual Schottky barrier (diode D_K) and a low tunnel-shunt resistance (R_K). In this configuration we expect that photocurrent generated at the diode D_J will
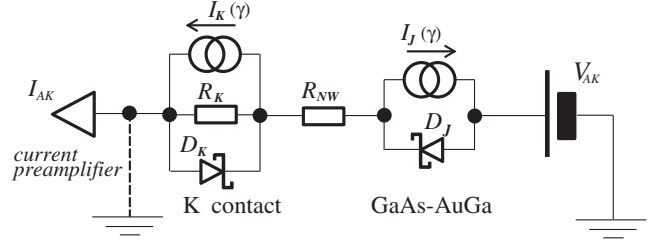
FIG. 4. *Photoconductivity model.* The device electrical response to photoexcitation can be explained by taking into account the bias-dependent resistance of the Schottky junction. At $V_{AK} \lesssim V_{th}$ the response is fully dominated by the charge separation of photoexcited pairs at the GaAs-AuGa junction, leading to an expected $\Delta I_{AK} \approx -I_J(\gamma)$ and to the strong negative photocurrent peak visible in Fig. 3. In this regime similar effects at the residual barrier at the K contact are strongly suppressed because of the small shunt resistance R_K, shorting the photocurrent inside the device, compared with the poor conductivity of D_J. Differently, for large V_{AK} the Schottky barrier becomes more conductive and a significant share of the photocurrent $I_K(\gamma)$ generated at the K contact can reach the outer portion of the circuit and have an impact on the measured excess current ΔI_{AK}.

almost completely reach the outer circuit and lead to an excess current $\Delta I_{AK} \approx -I_J(\gamma)$. Differently, any photocurrent $I_K(\gamma)$ generated at the K contact will be mostly shunted by R_K and will not impact the measured I_{AK}. The situation further evolves for large values of V_{AK}: the diode D_J becomes more and more conductive and a share of $I_K(\gamma)$ can thus reach the outer measurement circuit and lead to a positive photocurrent peak.

Additional effects are observed as a function of the V_{AK} bias. In particular, an unexpected positive PC response emerges when the laser is positioned on top of the AuGa phase and the diode is forward biased beyond the threshold. The origin of this effect is still unclear, but it is most probably *not* related to a mechanism of field-induced separation of photogenerated electron-hole pairs. The AuGa region is in fact strongly conductive [35] and no significant voltage drop nor electric field is expected in this region of the device. A speculative explanation can be laser-induced heating and a consequent increased device conductivity. This hypothesis requires a sizable larger laser absorption of the AuGa region of the NW, which might be possible as a consequence of plasmon resonances in this strongly conductive part of the nanostructure. At present, this interesting possibility remains speculative and goes beyond the scope of the present article. Its precise verification will require additional modeling and an investigation of the PC response as a function of the excitation energy.

III. CONCLUSIONS

In conclusion, we have demonstrated that thermal annealing can be used to fabricate nanoscale Schottky diodes embedded in GaAs NWs. The junction area

≈ 6000–7000 nm^2 implies a very small junction capacitance of a few aF and a potential impact on high-speed applications. Bias spectroscopy and a phenomenological thermoionic emission model leads to an estimated ideality factor in the range of $\eta = 2.3$–3.3 and a barrier of $\phi_B = 0.2$–0.35 eV. Nevertheless, the highly doped NWs used for the current devices are found to lead to sizable tunnel and/or surface leaks which are visible in the reverse breakdown regime. The interpretation of the full current diode in terms of thermoionic emission is thus likely to lead to an underestimate of the barrier height ϕ_B. The diode behavior is further investigated by PC mapping, the presence of a Schottky barrier is revealed at the GaAs-AuGa interface, and PC as a function of the bias highlighted a reversal of the electric field sign at $V_{AK} = 0.4$–0.5 V. The unipolar nature of the device is consistent with the absence of light emission in the forward bias regime, and with its presence in the reverse breakdown regime.

ACKNOWLEDGMENTS

[1] C. M. Lieber, Nanoscale science and technology: Building a big future from small things, MRS Bull. **28**, 486 (2003).

[2] C. Thelander, P. Agarwal, S. Brongersma, J. Eymery, L. F. Feiner, A. Forchel, M. Scheffler, W. Riess, B. J. Ohlsson, U. Gosele, and L. Samuelson, Nanowire-based one-dimensional electronics, Mater. Today **9**, 28 (2006).

[3] A. W. Dey, J. Svensson, M. Ek, E. Lind, C. Thelander, and L. E. Wernersson, Combining axial and radial nanowire heterostructures: Radial Esaki diodes and tunnel field-effect transistors, Nano Lett. **13**, 5919 (2013).

[4] M. Egard, S. Johansson, A. C. Johansson, K. M. Persson, A. W. Dey, B. M. Borg, C. Thelander, L.-E. Wernersson, and E. Lind, Vertical InAs nanowire wrap gate transistors with $f_t > 7$ GHz and $f_{max} > 20$ GHz, Nano Lett. **10**, 809 (2010).

[5] C. Thelander, L. E. Freoberg, C. Rehnstedt, L. Samuelson, and L.-E. Wernersson, Vertical enhancement-mode InAs nanowire field-effect transistor with 50-nm wrap gate, IEEE Electron Device Lett. **29**, 206 (2008).

[6] Y.-F.Lin and W. B. Jian, The impact of nanocontact on nanowire based nanoelectronics, Nano Lett. **8**, 3146 (2008).

[7] S. Roddaro, A. Pescaglini, D. Ercolani, L. Sorba, F. Giazotto, and F. Beltram, Hot-electron effects in InAs nanowire Josephson junctions, manipulation of electron orbitals in hard-wall InAs/InP nanowire quantum dots, Nano Res. **4**, 259 (2011).

[8] S. Roddaro, A. Pescaglini, D. Ercolani, L. Sorba, and F. Beltram, Manipulation of electron orbitals in hard-wall InAs/InP nanowire quantum dots, Nano Lett. **11**, 1695 (2011).

[9] S. Roddaro, D. Ercolani, M. A. Safeen, S. Suomalainen, F. Rossella, F. Giazotto, L. Sorba, and F. Beltram, Giant thermovoltage in single InAs nanowire field-effect transistors, Nano Lett. **13**, 3638 (2013).

[10] C. P. T. Svensson, T. Mårtensson, J. Treagårdh, C. Larsson, M. Rask, D. Hessman, L. Samuelson, and J. Ohlsson, Monolithic GaAs/InGaP nanowire light emitting diodes on silicon, Nanotechnology **19**, 305201 (2008).

[11] K. Tomioka, J. Motohisa, S. Hara, K. Hiruma, and T. Fukui, GaAs/AlGaAs core multishell nanowire-based light-emitting diodes on Si, Nano Lett. **10**, 1639 (2010).

[12] V. N. Trukhin, A. S. Buyskikh, N. A. Kaliteevskaya, A. D. Bourauleuv, L. L. Samoilov, Yu. B. Samsonenko, G. E. Cirlin, M. A. Kaliteevski, and A. J. Gallan, Terahertz generation by GaAs nanowires, Appl. Phys. Lett. **103**, 072108 (2013).

[13] A. Pitanti, D. Ercolani, L. Sorba, S. Roddaro, F. Beltram, L. Nasi, G. Salviati, and A. Tredicucci, InAs/InP/InSb Nanowires as Low Capacitance *n-n* Heterojunction Diodes, Phys. Rev. X **1**, 011006 (2011).

[14] M. S. Vitiello, D. Coquillat, L. Viti, D. Ercolani, F. Teppe, A. Pitanti, F. Beltram, L. Sorba, W. Knap, and A. Tredicucci, Room-temperature terahertz detectors based on semiconductor nanowire field-effect transistors, Nano Lett. **12**, 96 (2012).

[15] S. Roddaro, A. Fuhrer, P. Brusheim, C. Fasth, H. Q. Xu, L. Samuelson, J. Xiang, and C. M. Lieber, Spin States of Holes in Ge/Si Nanowire Quantum Dots, Phys. Rev. Lett. **101**, 186802 (2008).

[16] L. Romeo, S. Roddaro, A. Pitanti, D. Ercolani, L. Sorba, and F. Beltram, Electrostatic spin control in InAs/InP nanowire quantum dots, Nano Lett. **12**, 4490 (2012).

[17] F. Rossella, A. Bertoni, D. Ercolani, M. Rontani, L. Sorba, F. Beltram, and S. Roddaro, Nanoscale spin rectifiers controlled by the Stark effect, Nat. Nanotechnol. **9**, 997 (2014).

[18] J. P. DeGrave, A. L. Schmitt, R. S. Selinsky, J. M. Higgins, D. J. Keavney, and S. Jin, Spin polarization measurement of homogeneously doped Fe$_{1-x}$Co$_x$Si nanowries by Andreev reflection spectroscopy, Nano Lett. **11**, 4431 (2011).

[19] F. Glas, Critical dimensions for the plastic relaxation of strained axial heterostructures in free-standing nanowires, Phys. Rev. B **74**, 121302 (2006).

[20] M. W. Larsson, J. B. Wagner, M. Wallin, P. Håkansson, L. E. Fröberg, L. Samuelson, and L. R. Wallenberg, Strain mapping in free-standing heterostructured wurtzite InAs/InP nanowires, Nanotechnology **18**, 015504 (2007).

[21] M. de la Mata, C. Magén, P. Caroff, and J. Arbiol, Atomic scale strain relaxation in axial semiconductor III-V nanowire heterostructures, Nano Lett. **14**, 6614 (2014).

[22] M. T. Björk, B. J. Ohlsson, T. Sass, A. I. Persson, C. Thelander, M. H. Magnusson, K. Deppert, L. R. Wallenberg, and L. Samuelson, One dimensional steeplechase for electrons realized, Nano Lett. **2**, 87 (2002).

[23] D. Ercolani, F. Rossi, A. Li, S. Roddaro, V. Grillo, G. Salviati, F. Beltram, and L. Sorba, InAs/InSb nanowire

heterostructures grown by chemical beam epitaxy, Nanotechnology **20**, 505605 (2009).

[24] S. Roddaro, P. Caroff, G. Biasiol, F. Rossi, C. Bocchi, K. Nilsson, L. Fröberg, J. B. Wagner, L. Samuelson, L. E. Wernersson, and L. Sorba, Growth of vertical InAs nanowires on heterostructured substrates, Nanotechnology **20**, 285303 (2009).

[25] P. Caroff, J. B. Wagner, K. A. Dick, H. A. Nilsson, M. Jeppsson, K. Deppert, L. Samuelson, L. R. Wallenberg, and L. E. Wernersson, High-quality InAs/InSb nanowire heterostructures grown by metal-organic vapor-phase epitaxy, Small **4**, 878 (2008).

[26] B. Mandl, A. W. Dey, J. Stangl, M. Cantoro, L. E. Wernersson, G. Bauer, L. Samuelson, K. Deppert, and C. Thelander, Self-seeded, position-controlled InAs nanowire growth on Si: A growth parameter study, J. Cryst. Growth **334**, 51 (2011).

[27] M. T. Björk, H. Schmid, C. M. Breslin, L. Gignac, and H. Riel, InAs nanowire growth on oxide-masked ⟨111⟩ silicon, J. Cryst. Growth **344**, 31 (2012).

[28] Y. Wu, J. Xiang, C. Yang, W. Lu, and C. M. Lieber, Single-crystal metallic nanowires and metal/semiconductor nanowire heterostructures, Nature (London) **430**, 61 (2004).

[29] W. M. Weber, L. Geelhaar, A. P. Graham, E. Unger, G. S. Duesberg, M. Liebau, W. Pamler, C. Chéze, H. Riechert, P. Lugli, and F. Kreupl, Silicon-nanowire transistors with intruded nickel-silicide contacts, Nano Lett. **6**, 2660 (2006).

[30] M. Mongillo, P. Spathis, G. Katsaros, P. Gentile, M. Sanquer, and S. De Franceschi, Joule-assisted silicidation for short-channel silicon nanowire devices, ACS Nano **5**, 7117 (2011).

[31] M. Mongillo, P. Spathis, G. Katsaros, P. Gentile, and S. De Franceschi, Multifunctional devices and logic gates with undoped silicon nanowires, Nano Lett. **12**, 3074 (2012).

[32] W. Tang, S. A. Dayeh, S. T. Picraux, J. Y. Huang, and K.-N. Tu, Ultrashort channel silicon nanowire transistors with nickel silicide source/drain contacts, Nano Lett. **12**, 3979 (2012).

[33] Y.-C. Lin, Y. Chen, and Y. Huang, The growth and applications of silicides for nanoscale devices, Nanoscale **4**, 1412 (2012).

[34] S. Kral, C. Zeiner, M. Stöger-Pollach, E. Bertagnolli, M. I. den Hertog, M. Lopez-Haro, E. Robin, K. El Hajraoui, and A. Lugstein, Abrupt Schottky junctions in Al/Ge nanowire heterostructures, Nano Lett. **15**, 4783 (2015).

[35] M. Orrù, S. Rubini, and S. Roddaro, Formation of axial metalsemiconductor junctions in GaAs nanowires by thermal annealing, Semicond. Sci. Technol. **29**, 054001 (2014).

[36] Y. Chen, Y.-C. Lin, C.-W. Huang, C.-W. Wang, L.-J. Chen, W.-W. Wu, and Yu Huang, Kinetic competition model and size-dependent phase selection in 1-D nanostructures, Nano Lett. **12**, 3115 (2012).

[37] Y. Chen, Y.-C. Lin, X. Zhong, H.-C. Cheng, X. Duan, and Y. Huang, Kinetic manipulation of silicide phase formation in Si nanowire templates, Nano Lett. **13**, 3703 (2013).

[38] C. Colombo, M. Heiss, M. Grätzel, and A. Foncuberta i Morral, Gallium arsenide *p-i-n* radial structures for photovoltaic applications, Appl. Phys. Lett. **94**, 173108 (2009).

[39] K. Haraguchi, T. Katsuyama, K. Hiruma, and K. Ogawa, GaAs *p-n* junction formed in quantum wire crystals, Appl. Phys. Lett. **60**, 745 (1992).

[40] H. Wang, High gain single GaAs nanowire photodetector, Appl. Phys. Lett. **103**, 093101 (2013).

[41] D. B. Suyatin, V. Jain, V. A. Nebol'sin, J. Trägårdh, M. E. Messing, J. B. Wagner, O. Persson, R. Timm, A. Mikkelsen, I. Maximov, L. Samuelson, and H. Petterson, Strong Schottky barrier reduction at Au-catalyst/GaAs-nanowire interfaces by electric dipole formation and Fermi-level unpinning, Nat. Commun. **5**, 3221 (2014).

[42] A. G. Chynoweth and K. G. McKay, Photon emission from avalanche breakdown in silicon, Phys. Rev. **102**, 369 (1956).

[43] G. Masini, S. La Monica, G. Maiello, S. Lazarouk, and V. Bondarenko, White-light emission from porous-silicon-aluminum Schottky junctions, Il Nuovo Cimento D **18**, 1205 (1996).

[44] M. Balucani, S. La Monica, and A. Ferrari, 200 MHz optical signal modulation from a porous silicon light emitting device, Appl. Phys. Lett. **72**, 639 (1998).

[45] S. Ambrosini, M. Fanetti, V. Grillo, A. Franciosi, and S. Rubini, Vapor-liquid-solid and vapor-solid growth of self-catalyzed GaAs nanowires, AIP Adv. **1**, 042142 (2011).

[46] O. Wunnicke, Gate capacitance of back-gated nanowire field-effect transistors, Appl. Phys. Lett. **89**, 083102 (2006).

[47] See Supplemental Material at http://link.aps.org/supplemental/10.1103/PhysRevApplied.4.044010 for further information about the device transport parameters, additional results on photoconductivity, and light emission data.

[48] C. Gutsche, A. Lysov, I. Regolin, A. Brodt, L. Liborius, J. Frohleiks, W. Prost, and F.-J. Tegude, Ohmic contacts to n-GaAs nanowires, J. Appl. Phys. **110**, 014305 (2011).

[49] S. M. Sze, *Physics of Semiconductor Devices*, 2nd ed. (Wiley, New York, 1981).

[50] S.-Y. Lee and S.-K. Lee, Current transport mechanism in a metal-GaN nanowire Schottky diode, Nanotechnology **18**, 495701 (2007).

[51] Y. Calahorra, D. Mendels, and A. Epstein, Rigorous analysis of image force barrier lowering in bounded geometries: Application to semiconducting nanowires, Nanotechnology **25**, 145203 (2014).

[52] J. Sullivan, R. Tung, M. Pinto, and W. Graham, Electron transport of inhomogeneous Schottky barriers: A numerical study, J. Appl. Phys. **70**, 7403 (1991).

[53] M. Freitag, J. C. Tsang, A. Bol, D. Yuan, J. Liu, and P. Avouris, Imaging of the Schottky barriers and charge depletion in carbon nanotube transistors, Nano Lett. **7**, 2037 (2007).

[54] We note fringelike tail structures visible on the right side of the main peak of the PC maps at $V_{AK} = 0$ V and also visible in the profiles at $x \approx 0.5\ \mu$m in Fig. 3(a) are due to asymmetric diffraction and are not related to the device response (see Supplemental Material [47]). The dimension of these features is below the spatial resolution limited by the laser spot dimension.